Inter*net* Electronic Journal of Molecular Design

January 2005, Volume 4, Number 1, Pages 59–81

Editor: Ovidiu Ivanciuc

Periodic Properties of Carbon Nanotubes Based on the Chiral Vector

Francisco Torrens

Institut Universitari de Ciència Molecular, Universitat de València, Dr. Moliner 50, E–46100 Burjassot (València), Spain

Citation of the article:
F. Torrens, Periodic Properties of Carbon Nanotubes Based on the Chiral Vector, *Internet Electron. J. Mol. Des.* **2005**, *4*, 59–81, http://www.biochempress.com.

Periodic Properties of Carbon Nanotubes Based on the Chiral Vector

Francisco Torrens *

Institut Universitari de Ciència Molecular, Universitat de València, Dr. Moliner 50, E–46100 Burjassot (València), Spain

Abstract

Motivation. An earlier publication reported a periodic table (PT) for single–wall carbon nanotubes (SWNT). In the present study some properties are calculated with the aim of discussing PT format.

Method. The elementary polarizability $\langle\alpha\rangle$ and geometric, topological and solvation properties are computed because experimental properties depend on the sample, since some samples: (1) contain fullerenes, (2) consist of diameters d_t of metallic–semimetallic or semiconductor SWNTs, (3) show polydispersity between short and large SWNTs, (4) solubility of SWNTs differ for different d_t and (5) SWNTs thinner than (5,5) are scarce.

Results. The properties of SWNTs are related to the indices (n,m) designating the chiral vector. SWNTs are classified in zigzag $(n,0)$, armchair (n,n) and chiral (n,m). The properties allow classifying SWNTs according to (n,m). A recommended PT format is discussed.

Conclusions. The $\langle\alpha\rangle$ relationship of any SWNT (n,m) is similar to that of its neighbor $(n–1,m+1)$. The trend is approximately repeated for each period. Correlations between $(n^2+nm+m^2)^{1/2}$ and other properties show that (n,m) are adequate indices. The nanotube (10,10) is the favorite, presenting great kinetic stability and small $\langle\alpha\rangle$, pyramidalization angle, fractal index D_{cavity} and solubility, and great d_t, linear density, D, density and 1–octanol/cyclohexane/chloroform–water partition coefficients. SWNTs in some organic solvents are positively charged, while in water–Triton X are negative, what is explained on the basis of permittivity–electron affinity.

Availability. The original software used in the investigation is available from the author.

Keywords. Periodic table; carbon nanotube; polarizability; molecular globularity; molecular rugosity; solvent–accessible surface; fractal dimension; internal cavity; solubility; partition coefficient.

Abbreviations and notations

2D, two–dimensional	QSAR, quantitative structure–activity relationship
3D, three–dimensional	QSPR, quantitative structure–property relationship
AM, Austin model	R, radius
AS, water–accessible surface	r, correlation coefficient
AS', side–chain accessible surface	S, bare surface area
D, fractal–like index of the solvent–accessible surface	s, standard deviation
D', fractal–like index, averaged for non–buried atoms	SDS, sodium dodecylsulphate
d_t, diameter	S_w, solubility in water
EA, electron affinity	SWNT, single–wall carbon nanotube
F, variance ratio	V, volume
G, globularity	$\Delta G_{solv,cf}$, Gibbs free energy of solvation in chloroform

* Correspondence author; E–mail: Francisco.Torrens@uv.es.

G', rugosity	$\Delta G_{solv,ch}$, Gibbs free energy of solvation in cyclohexane
I, ionization potential	$\Delta G_{solv,o}$, Gibbs free energy of solvation in 1–octanol
N, number of data points	$\Delta G_{solv,w}$, Gibbs free energy of solvation in water
ODCB, *ortho*–dichlorobenzene	$<\alpha>$, elementary static dipole–dipole polarizability
p, position in the periodic table	ε, relative dielectric permittivity
P_o, 1–octanol–water partition coefficient	ϕ, bond angle
P_{cf}, chloroform–water partition coefficient	ρ, radial spherical coordinate
P_{ch}, cyclohexane–water partition coefficient	ρ_l, linear density
PT, periodic table	ρ_t, density
Pyr, pyramidalization angle averaged for trivalent atoms	θ, pyramidalization angle averaged for trivalent atoms

1 INTRODUCTION

Inspired by the periodic table (PT) of the elements [1], several PTs can be suggested: of relativistic effects [2] and molecules (alkanes [3,4], acyclic hydrocarbons [5,6], polycyclic aromatic hydrocarbons [7,8], benzenoid hydrocarbons [9], fullerenes [10,11], helicenes [12] and local anaesthetics [13]). The analysis of the physics of the arc plasma indicated that the growth of single–wall carbon nanotubes (SWNT) is the result of the competition between two types of carbon species present near the cathode: the anisotropic unidirectional carbon ions accelerated across the gap, and thermally evaporated carbon from the cathode with isotropic velocity distribution [14]. Self–assembly of fullerenes [15] and SWNTs is a sharp demonstration of the classical crystal physics of nucleation and growth. In a graphite–rod arc discharge [16] or during laser ablation [17], energetic C atoms comprising a dense neutral gas ($T \geq T_F \sim 5600$ K) undergo repeated nearest–neighbor collisions, which become more sticky during normal three–dimensional (3D) system cooling [18]. In this vapor process of homogeneous C_{60} nucleation colliding C_1, C_2, C_3 *etc*. are ultimately self–trapped into transient growing molecular C_n nuclei, whose size and form are essentially determined by the C–C bond. In a time ~2500ps an essentially two–dimensional (2D) pentagon becomes the base for corannulene C_{20}–bowl in 3D [19], developing swiftly by edge/step accretion into C_{30}–hemisphere, which rapidly closes into C_{60}–I_h. SWNTs and other nanoclusters were grown controllably by simple surface self–diffusion, both homogeneous and heterogeneously, following a mechanical ball–milling preparative stage [20]. Fullerenic SWNTs were produced by condensation of a laser–vaporized C–Ni–Co mixture at 1200 ºC [21]. X–ray diffraction and electron microscopy showed that these SWNTs are nearly uniform in diameter d_t, and that they self–organize into ropes, which consist of 100–500 SWNTs in a 2D triangular lattice with a lattice constant of 17 Å. The X–ray form factor is consistent with that of uniformly charged cylinders $d_t = (13.8\pm0.2)$ Å. The ropes were metallic, with a single–rope resistivity of $<10^{-4} \cdot \Omega \cdot$cm at 300 K. The uniformity of SWNT d_t is attributed to the efficient annealing of an initial fullerenic tubelet kept open by a few metal atoms; the optimum d_t is determined by competition between the strain energy of curvature of the graphene sheet and dangling–bond energy of the open edge, where growth occur. These factors strongly favor the metallic (10,10)–C_{5v} SWNT and an open edge stabilized by C≡C bonds.

The simplest way of specifying the structure of a SWNT is in terms of the chiral vector **C**, *i.e.*

the lattice vector on the graphene lattice. The cylinder is produced by rolling the sheet such that the two end–points of the vector are superimposed. Because of the symmetry of the honeycomb lattice, many of the cylinders produced in this way will be equivalent, but there is an irreducible wedge comprising one twelfth of the graphene lattice, within which unique SWNT structures are defined. Each pair of integers (n,m) represents a possible structure. $\mathbf{C}$ can be expressed as $\mathbf{C} = n\,\mathbf{a}_1 + m\,\mathbf{a}_2$, where $\mathbf{a}_1$ and $\mathbf{a}_2$ are the unit cell base vectors of graphene, and $n \geq m$. SWNTs can be classified in three types, *viz.* zigzag ($m = 0$), armchair ($n = m$), and chiral (n,m). Since $|\mathbf{a}_1| = |\mathbf{a}_2| = 2.46$ Å, the magnitude of $\mathbf{C}$ in ångströms is $C = 2.46(n^2 + nm + m^2)^{1/2}$, and the diameter is given by:

$$d_t = \frac{C}{\pi} = 0.783\left(n^2 + nm + m^2\right)^{1/2} \tag{1}$$

The linear density in atoms per ångström is given by:

$$\rho_l = \frac{4C}{3^{1/2} a^2} = 0.939\left(n^2 + nm + m^2\right)^{1/2} \tag{2}$$

When $n - m = 3q$, where q is an integer, SWNT is metallic or semimetallic, and the remaining species are semiconducting with a geometry–dependent bandgap.

The scientific interest of PT for SWNTs is: (1) to predict periodic properties of SWNTs, especially for scarce SWNTs, *e.g.*, (4–8,0) and (2,2)–(4,4); (2) to understand the abundance of different SWNTs; and (3) to understand the solubility and partition properties of SWNT suspensions. The impact of PT is: (1) That PT provides the framework for understanding the limits of what one knows and can learn about SWNTs. This epistemology represents an important goal in deciphering the information content of chiral–vector formulas. (2) That it provides a useful device for classifying SWNT types. (3) The characterization of different SWNTs. Possible applications of PT are: (1) separation of fullerenes/SWNTs, short/large SWNTS and thin/thick SWNTs, (2) to separate, manipulate and purify SWNT suspensions in water, and (3) to transform long into short SWNTs. The objective is: (1) to render SWNTs soluble in organic and, especially, aqueous solutions; (2) to form SWNT suspensions in water, especially without surfactants; (3) to permit extracting SWNTs from a suspension with a second solvent; (4) to make SWNTs non–toxic and biocompatible; (5) to integrate SWNTs in biosystems without functionalization; and (6) PT positions provide some guidance in the areas of experimental or theoretical chemistry that are concerned with the most likely candidates that posses an extreme degree of the property of interest, *e.g.*, in quantitative structure–property relationships (QSPR) and quantitative structure–activity relationships (QSAR). Possible predictions of PT are: (1) the stability of SWNTs, *e.g.*, scarce SWNTs as those thinner than (5,5); (2) the elucidation of the thinnest SWNT, perhaps (2,2) of 3Å width [22]; and (3) whether and how SWNTs are capped. In earlier publications, PTs for fullerenes [23,24] and SWNTs [25] were reported. In the present study some properties for SWNTs are calculated with the aim of discussing PT format. Section 2 presents the methods. Section 3 discusses the results. Section 4 summarizes the conclusions.

2 MATERIALS AND METHODS

Program TOPO [26] represents the surface of molecules by the external surface of a set of overlapping spheres with appropriate radii [27], centered on the nuclei of the atoms [28,29]. The molecule is treated as a solid in space defined by tracing spheres about the atomic nuclei. It is enclosed in a box and the geometric descriptors evaluated by counting points within the solid or close to chosen surfaces. The molecular volume is calculated as $V = P \cdot \text{GRID}^3$, where P is the number of points within the molecular volume and GRID is the size of the mesh grid. The molecular bare surface area could be estimated as $S = Q \cdot \text{GRID}^2$, where Q is the number of points close to the bare surface area (within a distance between R_X and $R_X + \text{GRID}$ of any atomic nucleus X). If the point falls exactly on the surface of one of the atomic spheres, it accounts for GRID^2 units of area on the molecular bare surface. This is because the total surface of atom X can accommodate $4\pi \cdot R_X^2 / \text{GRID}^2$ points. When a point falls beyond the surface, it represents GRID^2 units of area on the surface of a sphere of radius $R > R_X$, not on the surface of atom X. On the surface of X it accounts only for a fraction of this quantity: $\text{GRID}^2 (R_X / R)^2$. The total bare surface area is calculated now as $S = F \cdot \text{GRID}^2$, where F is the sum of elements AF defined as $\text{AF} = R_X^2 / R^2(I)$ for those points close enough to the surface of any atom X. R_X^2 is the squared radius of atom X and $R^2(I)$ is the squared distance of point I from the atomic nucleus X. If S_e is the surface area of a sphere whose volume is equal to the molecular volume V, the ratio $G = S_e / S$ is interpreted as a descriptor of molecular globularity. The ratio $G' = S/V$ is interpreted as a descriptor of molecular rugosity. The solvent–accessible surface (AS) is calculated in the same way as S by mean of pseudoatoms, whose van der Waals radii are increased by the radius R of the probe. The accessibility is a dimensionless quantity varying between 0 and 1, which represents the ratio of the accessible surface area in a particular structure to the accessible surface area of the same atom when isolated from the molecule. The fractal–like index D [30] is obtained as

$$D = 2 - \frac{d(\log \text{AS})}{d(\log R)} \tag{3}$$

where R is the probe radius [31]. A version of TOPO has been implemented in programs AMYR [32], SURMO2 and GEPOL.

Program SURMO2 represents the global shape of a molecule as an envelope of the van der Waals spheres of the external atoms [33]. This allows a numerical treatment of integrals defined on the molecular surface as

$$I = \int g(\rho, \theta, \phi) d\omega \tag{4}$$

where g is the position vector of a point in the surface and $d\omega = \sin\theta \, d\theta \, d\phi$ represents the elementary solid angle. The evaluation of the Eq. (4)–type integrals is obtained from the finite sum $I = \int g d\omega \approx \sum_i g_i \delta\omega_i$. To achieve the summation one can take a mesh of points $M_{ij}(\theta_i, \phi_j)$ by cutting

the surfaces on a single unitary sphere with a uniform distribution of $2N_1$ parallels and N_2 meridians. If the molecule is cut by an axis passing by the origin, two intersecting points are obtained: g^+ and g^-. Denoting by M_0 the upper pole, M_{1j} the points placed on the first parallel, M_{ij} those of the *i–th* parallel and $M_{N_1 j}$ those placed on the equator, the integral (4) can be measured as

$$I = \frac{N_2}{3}\left(g^+_{M_0} + g^-_{M_0}\right) + \frac{7}{6}\sum_{j=0}^{N_2-1}\left(g^+_{M_{1j}} + g^-_{M_{1j}}\right) + \frac{1}{2}\sum_{j=0}^{N_2-1}\left(g^+_{M_{N_1 j}} + g^-_{M_{N_1 j}}\right) + \sum_{i=2}^{N_1-1}\sum_{j=0}^{N_2-1}\left(g^+_{M_{ij}} + g^-_{M_{ij}}\right) \qquad (5)$$

where $\sum_j g_{M_{ij}}$ indicates a sum over all of the mesh points on the *i–th* parallel. The molecular volume is calculated as

$$V = \frac{1}{3}\int \rho^3 d\omega = \frac{4\pi}{3 \cdot 2N_1 N_2}\sum_{i=0}^{N_1} r_{M_i}\sum_{j=0}^{N_2-1}\left[\left(g^+_{M_{ij}}\right)^3 + \left(g^-_{M_{ij}}\right)^3\right] \qquad (6)$$

where ρ is the radial spherical coordinate, $r = (1/3, 7/6, 1, 1,\dots,1/2)$ and Eq. (5) has been used. The molecular surface area S is calculated as:

$$S = \int \rho^2 d\omega = \frac{4\pi}{2N_1 N_2}\sum_{i=0}^{N_1} r_{M_i}\sum_{j=0}^{N_2-1}\left[\left(g^+_{M_{ij}}\right)^2 + \left(g^-_{M_{ij}}\right)^2\right] \qquad (7)$$

The calculation of S has been improved by dividing each g^2 by the cosine of the angle formed by the semiaxis and normal vector:

$$S = \frac{4\pi}{2N_1 N_2}\sum_{i=0}^{N_1} r_{M_i}\sum_{j=0}^{N_2-1}\frac{\left(g^+_{M_{ij}}\right)^2 + \left(g^-_{M_{ij}}\right)^2}{\cos\alpha_{M_{ij}}} \qquad (8)$$

Program GEPOL sets a sphere on each atom and creates new spheres in the spaces inaccessible to the solvent [34]. Their spherical surfaces are divided into a set of triangular tessels using a pentakis dodecahedron. The division can be increased *via* tessellation parameter NDIV. The molecular surface area is obtained summing the areas of all triangles: $S = \sum_i S_i$, where S_i is the area of the *i–th* triangle. Let $\mathbf{r}_i$ be the position vector of the *i–th* triangle center, and $\mathbf{n}_i$ be the corresponding vector normal to the surface at this point. The volume is obtained by summing all solid volumes made by the triangles vector surfaces and the origin of the molecule: $V = (1/3)\sum_i S_i \mathbf{n}_i \bullet \mathbf{r}_i$. GEPOL has been used for reference calculations. TOPO and GEPOL recognize the internal cavities in SWNTs. However, SURMO2 does not recognize the cavities.

3 RESULTS AND DISCUSSION

In earlier publications a PT of (*n,m*) SWNTs classified them by *n* and *m* [25]. In this study an extension of the PT approach for SWNTs is reported. The elementary polarizability per atom $\langle\alpha\rangle$ has been calculated with program PAPID [35] for (*n*,0) zigzag and (*n,n*) armchair SWNTs, with the number of C atoms varying from 16 to 200 for *n* = 4 to 20 [36,37]. Molecular geometries have been

optimized with MMID2. The radius of SWNT, R increases with the number of rings around a section of SWNT, n. In general the calculated $<\alpha>$ increases monotonically with R. In particular, for (9,0) the computed $<\alpha>_{C90} = 1.130\text{Å}^3$ is similar to the reference *ab initio* calculation $<\alpha>_{C90} = 1.304\text{Å}^3$ [38], improving the agreement for shorter (9,0): $<\alpha>_{C72} = 1.132\text{Å}^3$, $<\alpha>_{C54} = 1.220\text{Å}^3$ and $<\alpha>_{C36} = 1.361\text{Å}^3$. The variation of $<\alpha>$ with the radius of $(n,0)$ n from 9–18 SWNTs C_{90}–C_{180} fits to:

$$\frac{1}{\langle \alpha \rangle} = a + \frac{b}{R} \tag{9}$$

where a is the inverse $<\alpha>$ of graphene. The calculated polarizabilities are:

$$\frac{1}{\langle \alpha \rangle_{(n,0)}} = 0.721 + \frac{0.595}{R} \quad N = 10 \ \ r = 0.992 \ \ s = 0.004 \ \ F = 520.6 \tag{10}$$

and $<\alpha>_{graphene}$ extrapolates as 1.388Å^3. Calculated $<\alpha>_{(n,0)}$ with $n \leq 8$ deviates from the above simple scaling, perhaps due to the fact that the singlet π^* band, which is normally in the conduction band, falls into the band gap as a result of increased σ^*–π^* mixing at high curvature [39]. Increasing $<\alpha>$ with decreasing R shows that, for small R, the character of the surface deviates from that of graphene, suggesting that creating regions of different curvature on a single SWNT by radial deformation, one can attain different values for $<\alpha>$. For (n,n) n from 5–10 SWNTs C_{100}–C_{200} the variation of the calculated $<\alpha>$ with R is:

$$\frac{1}{\langle \alpha \rangle_{(n,n)}} = 0.742 + \frac{0.485}{R} \quad N = 6 \ \ r = 0.989 \ \ s = 0.004 \ \ F = 185.1 \tag{11}$$

and $<\alpha>_{graphene}$ extrapolates as 1.348Å^3.

The values for $<\alpha>$ allow the format presented in Table 1 for PT of (n,m) SWNTs. SWNTs are classified by n and m, *e.g.*, group m0 ($m = 0$) includes the $(n,0)$ SWNTs; group m5 ($m = 5$) comprises the $(n,5)$ SWNTs. Periods of $(n + 1)/2$ (n odd) and $(n + 2)/2$ (n even) units are assumed because $n \geq m$. SWNTs in the same row (period) of Table 1 show close values of $<\alpha>$. In general $<\alpha>$ increases from top to bottom and from left to right. In particular $<\alpha>_{(10,10)}$ is almost the greatest for all SWNTs. $<\alpha>_{(n,0)–(n,n)}$ correlate well with $(n^2+nm+m^2)^{1/2}$. For C_{90}–C_{180} the variation of $<\alpha>_{(n,0)}$ with $(n^2+nm+m^2)^{1/2}$ is:

$$\langle \alpha \rangle_{(n,0)} = 1.013 + 0.0133\left(n^2 + nm + m^2\right)^{1/2} \quad N = 10 \ \ r = 0.998 \ \ s = 0.002 \ \ F = 2427.4 \tag{12}$$

For C_{100}–C_{200} the variation of $<\alpha>_{(n,n)}$ with $(n^2+nm+m^2)^{1/2}$ is:

$$\langle \alpha \rangle_{(n,n)} = 1.036 + 0.0117\left(n^2 + nm + m^2\right)^{1/2} \quad N = 6 \ \ r = 0.999 \ \ s = 0.002 \ \ F = 2968.6 \tag{13}$$

The slope of the $(n,0)$ curve is slightly larger than that of the (n,n) curve. For thinner SWNTs calculated $<\alpha>_{(n,0)}$ is smaller than $<\alpha>_{(n,n)}$. However, this trend is reversed after $R = 5.4\text{Å}$ for (8,8)–(14,0) and thicker SWNTs. $<\alpha>_{(10,10)} = 1.237\text{Å}^3$ is: (1) slightly smaller than that interpolated from

the (n,n) fit $<\alpha>_{(10,10),int} = 1.239$ Å^3, Eq. (13), (2) slightly smaller than that of the closer (17,0) $<\alpha>_{(17,0)} = 1.239$ Å^3, and (3) rather smaller than that of (18,0) $<\alpha>_{(18,0)} = 1.249$ Å^3, and smaller than those extrapolated for (19,0)–(20,0).

Table 1. Periodic Table of Nanotubes Based on Chiral Vector. Calculated–Differential Elementary Polarizability (Å) [a]

m0	m1	m2	m3	m4	m5	m6	m7	m8	m9	m10
(9,0)	(8,1)	(7,2)	(6,3)	(5,4)	–	–	–	–	–	–
1.130	1.076	1.089	1.119	1.096						
−0.054	**0.013**	*0.030*	−0.023	0.049						
(10,0)	(9,1)	(8,2)	(7,3)	(6,4)	(5,5)	–	–	–	–	–
1.145	1.122	1.090	1.096	1.094	1.136					
−0.023	−0.032	**0.006**	−0.002	0.042	0.024					
(11,0)	(10,1)	(9,2)	(8,3)	(7,4)	(6,5)	–	–	–	–	–
1.160	1.139	1.099	1.098	1.109	1.104					
−0.021	−0.040	−0.001	**0.011**	**−0.005**	0.071					
(12,0)	(11,1)	(10,2)	(9,3)	(8,4)	(7,5)	(6,6)	–	–	–	–
1.175	1.127	1.099	1.098	1.089	1.114	1.158				
−0.048	−0.028	−0.001	−0.009	0.025	0.044	0.031				
(13,0)	(12,1)	(11,2)	(10,3)	(9,4)	(8,5)	(7,6)	–	–	–	–
1.189	1.112	1.110	1.120	1.113	1.134	1.123				
−0.077	−0.002	**0.010**	−0.007	0.021	**−0.011**	0.079				
(14,0)	(13,1)	(12,2)	(11,3)	(10,4)	(9,5)	(8,6)	(7,7)	–	–	–
1.202	1.116	1.105	1.128	1.127	1.143	1.139	1.179			
−0.086	−0.011	*0.023*	−0.001	0.016	**−0.004**	0.040	0.036			
(15,0)	(14,1)	(13,2)	(12,3)	(11,4)	(10,5)	(9,6)	(8,7)	–	–	–
1.215	1.120	1.161	1.133	1.144	1.113	1.129	1.154			
−0.095	*0.041*	−0.028	**0.011**	*−0.031*	0.016	0.025	0.073			
(16,0)	(15,1)	(14,2)	(13,3)	(12,4)	(11,5)	(10,6)	(9,7)	(8,8)	–	–
1.227	1.133	1.156	1.153	1.142	1.152	1.156	1.156	1.200		
−0.094	*0.023*	−0.003	−0.011	0.010	0.004	0.000	0.044	0.039		
(17,0)	(16,1)	(15,2)	(14,3)	(13,4)	(12,5)	(11,6)	(10,7)	(9,8)	–	–
1.239	1.147	1.166	1.156	1.161	1.165	1.179	1.169	1.171		
−0.092	**0.019**	−0.010	**0.005**	0.004	0.014	**−0.010**	0.002	0.078		
(18,0)	(17,1)	(16,2)	(15,3)	(14,4)	(13,5)	(12,6)	(11,7)	(10,8)	(9,9)	–
1.249	1.166	1.170	1.176	1.161	1.165	1.141	1.192	1.166	1.219	
−0.083	**0.004**	**0.006**	−0.015	0.004	*−0.024*	0.051	*−0.026*	0.053	−0.082	
(19,0)	(18,1)	(17,2)	(16,3)	(15,4)	(14,5)	(13,6)	(12,7)	(11,8)	(10,9)	–
1.137	1.192	1.174	1.187	1.180	1.183	1.192	1.195	1.193	1.197	
0.055	−0.018	**0.013**	−0.007	0.003	0.009	0.003	**−0.002**	0.004	−0.046	
(20,0)	(19,1)	(18,2)	(17,3)	(16,4)	(15,5)	(14,6)	(13,7)	(12,8)	(11,9)	(10,10)
1.151	1.182	1.189	1.182	1.188	1.179	1.197	1.199	1.180	1.211	1.237
0.031	**0.007**	−0.007	**0.006**	−0.009	0.018	0.002	**−0.019**	0.031	*0.026*	–

[a] Values whose sign is opposite to that in its group are boldfaced; exceptions reaching 2% are italicized

If a function $<\alpha>(p)$ is assumed for a given position in PT, p, a maximum value $<\alpha>_{max}(p)$ for a given value of p has meaning only if it is compared with those for the former $<\alpha>(p-1)$ and later $<\alpha>(p+1)$ points, needing to fulfill:

$$\langle\alpha\rangle_{max}(p) > \langle\alpha\rangle(p-1)$$
$$\langle\alpha\rangle_{max}(p) > \langle\alpha\rangle(p+1)$$

(14)

Conditions (14) are order relationships, being these connections precisely what, the periodic law (PL) being fulfilled, should repeat at determined intervals equal to the values of the size of the

periods. Expressions (14) are equivalent to:

$$\langle\alpha\rangle_{max}(p)-\langle\alpha\rangle(p-1)>0$$
$$\langle\alpha\rangle(p+1)-\langle\alpha\rangle_{max}(p)<0 \tag{15}$$

As expressions (15) are valid only for the maxims of $<\alpha>(p)$, more general others are desired for all the values of p. Therefore, the differences $<\alpha>(p+1) - <\alpha>(p)$ are calculated assigning each of their values to SWNT p. Naming this value $D(p)$, one has:

$$D(p)=\langle\alpha\rangle(p+1)-\langle\alpha\rangle(p) \tag{16}$$

If PL were general, the elements belonging to the same group will satisfy identical relationship:

$$D(p)>0 \text{ or } D(p)<0 \tag{17}$$

Nevertheless, the results show that this is not the case, so that PL is not general, existing some anomalies. If coherence were rigorous $<\alpha>$ will have the same sign for all SWNTs in each group. However, in detail there are anomalies in the SWNTs for the successive periods. Furthermore, the mean absolute error of the exceptions is 1.4%.

Table 2. Geometric Descriptors for Single–Wall Carbon Nanotube Fragments

Nanotube	d_t[a]	ρ_l[b]	Pyr[c]	V[d]	V Ref.[e]	S[f]	S Ref.[e]	AS[g]	AS Ref.[e]	AS'[h]	AS' Ref.[e]
90 (9,0)	7.046	8.451	5.766	797	806	650	686	802	823	1267	1279
100 (10,0)	7.829	9.390	5.191	886	894	723	761	892	919	1350	1364
110 (11,0)	8.612	10.329	4.720	975	985	796	839	983	1009	1437	1450
120 (12,0)	9.395	11.268	4.327	1064	1074	867	915	1073	1100	1526	1538
130 (13,0)	10.178	12.207	3.995	1153	1164	939	993	1163	1193	1619	1635
140 (14,0)	10.960	13.146	3.710	1242	1254	1014	1070	1258	1286	1733	1757
150 (15,0)	11.743	14.085	3.463	1330	1343	1085	1145	1344	1376	1864	1886
160 (16,0)	12.526	15.023	3.246	1419	1434	1158	1223	1434	1470	1983	2009
170 (17,0)	13.309	15.962	3.055	1507	1523	1230	1300	1523	1563	2109	2135
180 (18,0)	14.092	16.901	2.886	1597	1612	1302	1377	1611	1655	2232	2260
100 (5,5)	6.780	8.132	5.991	883	892	707	748	847	877	1343	1357
120 (6,6)	8.136	9.758	4.995	1061	1072	851	900	1020	1049	1490	1502
140 (7,7)	9.492	11.384	4.282	1238	1250	993	1050	1194	1227	1652	1666
160 (8,8)	10.848	13.011	3.748	1415	1430	1138	1202	1365	1404	1840	1857
180 (9,9)	12.204	14.637	3.332	1592	1609	1282	1354	1538	1577	2068	2093
200 (10,10)	13.560	16.263	2.999	1769	1789	1424	1504	1707	1762	2302	2333

[a] Molecular diameter (Å)
[b] Linear density (atoms·Å^{-1})
[c] Pyramidalization angle averaged for trivalent atoms (º)
[d] Molecular volume (Å^3)
[e] Reference: calculations carried out with the GEPOL program
[f] Molecular surface area (Å^2)
[g] Water–accessible surface area (Å^2)
[h] Side–chain accessible surface area (Å^2)

Table 2 gives the diameter d_t for $(n,0)$–(n,n) SWNTs calculated *via* Eq. (1). The maximum $d_{t(18,0)}$ is similar to that for the competitive (10,10). Figure 1 illustrates the diameter d_t *vs.* $(n^2+nm+m^2)^{1/2}$. In particular $d_{t(10,10)}$ is slightly greater than that of the closer (17,0).
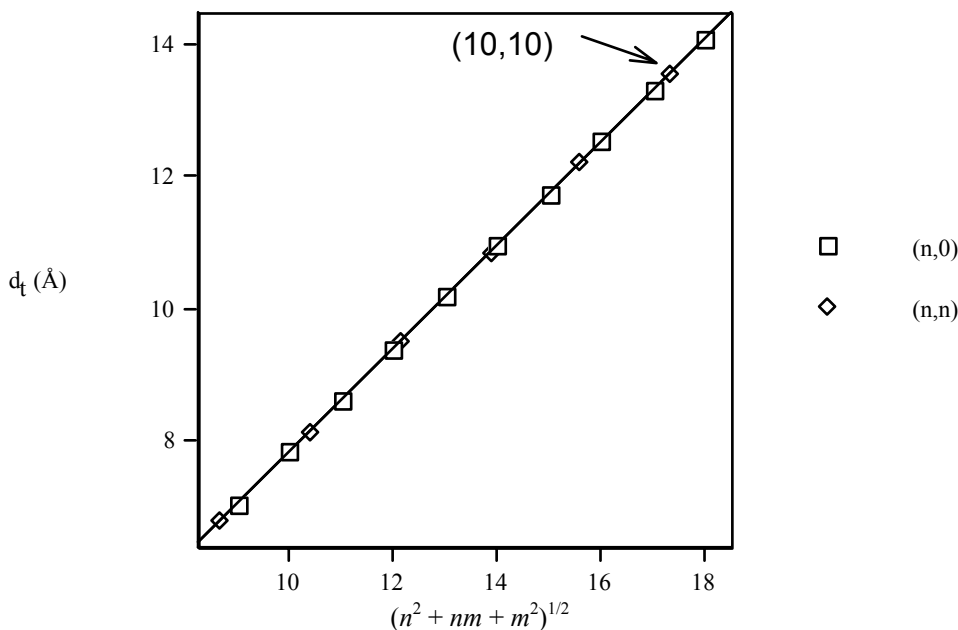
Figure 1. Variation of molecular diameter *vs.* $(n^2 + nm + m^2)^{1/2}$.

Table 2 gives the linear density ρ_l for $(n,0)$–(n,n) SWNTs calculated *via* Eq. (2). The maximum $\rho_{l(18,0)}$ is similar to that of the competitive (10,10). Figure 2 illustrates the density ρ_l *vs.* $(n^2 + nm + m^2)^{1/2}$. In particular $\rho_{l(10,10)}$ is slightly greater than that of the closer (17,0).
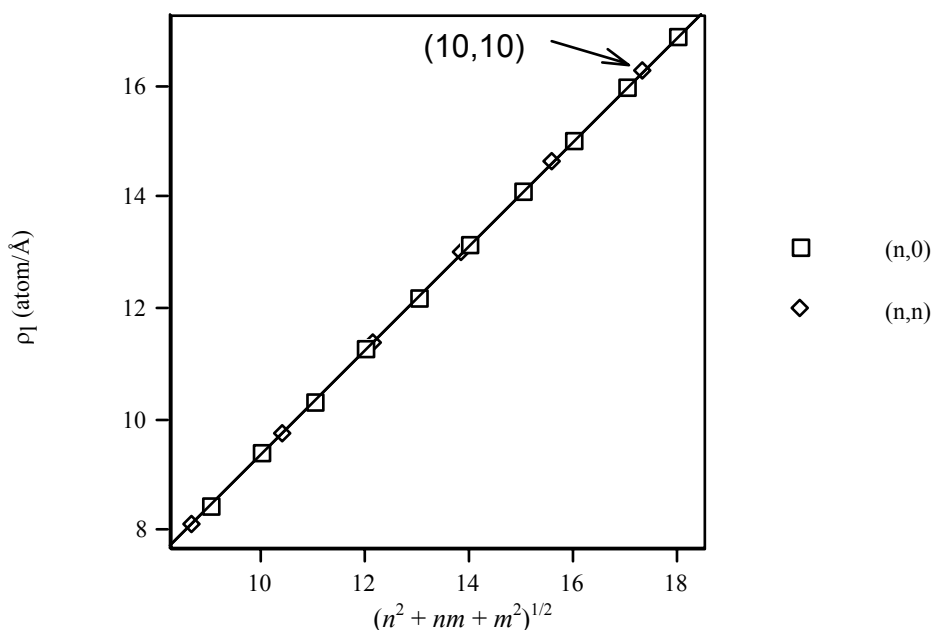
Figure 2. Variation of molecular linear density *vs.* $(n^2 + nm + m^2)^{1/2}$.

The pyramidalization angle θ averaged for the trivalent C atoms (*cf.* Table 2) decreases monotonically from (9,0) to (18,0), and from (5,5) to (10,10). SWNT chemistry was described with a pyramidalization angle formalism [40]. Chemical reactivity and kinetic selectivity are related to the extent of *s* character due to the curvature–induced strain of the sp^2–hybridized graphene sheet.

Because strain energy per carbon is inversely related to SWNT diameter, this model predicts that thinner SWNTs will be the most reactive, with the enthalpy of reaction decreasing as the curvature becomes infinite. The pyramidalization angles can be compared with those of fullerenes, which decrease from C_{60}–I_h (12.0˚), C_{70}–D_{5h} (11.2˚), C_{80}–I_h (10.4˚), C_{90}–C_{2v} (10.0˚), C_{100} (9.6˚), C_{240}–I_h (5.8˚), C_{500}–I_h (4.0˚) to C_{1000} (2.8˚). Although fullerenes and SWNTs are both examples of curved carbon, there are significant structural differences that are expected to be reflected in their chemistry, *i.e.*, fullerenes are curved in 2D whereas SWNTs are curved in one dimension. For a curved carbon structure of given radius, C atoms in a fullerene are more distorted than those in the corresponding SWNT are, *e.g.*, to curve a graphene sheet into $SWNT_{(10,10)}$ requires a pyramidalization angle of ≈3.0º, whereas the fullerene of equivalent radius, C_{240} [$SWNT_{(10,10)}$ can be capped by a hemisphere of C_{240}], has $\theta = 5.8º$; to curve a graphene sheet into $SWNT_{(5,5)}$ requires $\theta \approx 6.0º$, whereas the fullerene of equivalent radius, C_{60} [$SWNT_{(5,5)}$ can be capped by a hemisphere of C_{60}], has $\theta = 12.0º$. The strain energy of pyramidalization is roughly proportional to θ^2, so the fullerene must absorb ≈10 times the strain energy of pyramidalization per C atom, compared to the equivalent SWNT at these diameters. The minimum $\theta_{(18,0)}$ is similar to that of the competitive (10,10). Figure 3 displays the pyramidalization angle θ for $(n,0)$–(n,n) *vs.* $(n^2+nm+m^2)^{-1/2}$. θ of thinner SWNTs is calculated greater than those of thicker SWNTs are. Both representations correlate well with $(n^2+nm+m^2)^{-1/2}$. The variation of $\theta_{(n,0)}$ with $(n^2+nm+m^2)^{-1/2}$ is:

$$\theta_{(n,0)} = 0.00579 + 51.9\left(n^2 + nm + m^2\right)^{-1/2} \qquad (18)$$
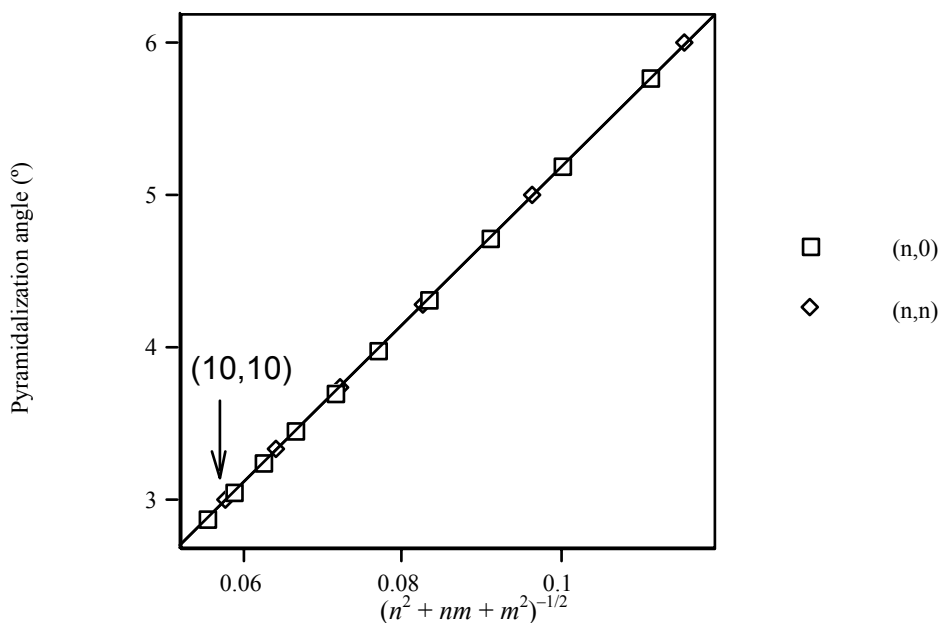
Figure 3. Variation of pyramidalization angle averaged for trivalent atoms *vs.* $(n^2 + nm + m^2)^{-1/2}$.

The variation of $\theta_{(n,n)}$ with $(n^2+nm+m^2)^{-1/2}$ is:

$$\theta_{(n,n)} = 0.00754 + 51.8\left(n^2 + nm + m^2\right)^{-1/2} \qquad (19)$$

In particular $\theta_{(10,10)}$ is almost the smallest for all SWNTs.

The remaining geometric descriptors in Table 2 have been calculated with TOPO. The volume and surface areas of SWNTs increase with *n* and *m*. Reference calculations have been carried out with GEPOL. The comparison between GEPOL and TOPO is of especial interest because the former does not perform an atom–to–atom analysis of the geometric descriptors of the molecules. For the molecular volume and surface areas there is good agreement between TOPO and GEPOL. Errors are ≈–1% for the molecular volume, ≈–5% for the bare molecular surface, ≈–3% for the water–accessible surface and ≈–1% for the side–chain accessible surface areas. In particular $V_{(10,10)}$, $S_{(10,10)}$, $AS_{(10,10)}$ and $AS'_{(10,10)}$ are maxims.

Table 3. Topological Indices for Single–Wall Carbon Nanotube Fragments

Nanotube	G [a]	G Ref. [b]	G' [c]	G' Ref. [b]	D [d]	D Ref. [b]	D' [e]
90 (9,0)	0.640	0.611	0.815	0.851	1.555	1.570	1.572
100 (10,0)	0.617	0.590	0.816	0.851	1.602	1.620	1.623
110 (11,0)	0.597	0.570	0.817	0.852	1.643	1.655	1.667
120 (12,0)	0.581	0.554	0.815	0.852	1.664	1.679	1.691
130 (13,0)	0.566	0.539	0.815	0.853	1.681	1.694	1.712
140 (14,0)	0.551	0.526	0.816	0.853	1.690	1.696	1.723
150 (15,0)	0.539	0.514	0.816	0.853	1.683	1.695	1.714
160 (16,0)	0.527	0.503	0.817	0.853	1.685	1.698	1.718
170 (17,0)	0.517	0.492	0.816	0.853	1.686	1.695	1.718
180 (18,0)	0.507	0.483	0.816	0.854	1.684	1.697	1.717
∞ (∞,0) extrapolation	0.425	0.404	0.817	0.856	1.685	1.696	1.717
100 (5,5)	0.630	0.599	0.800	0.838	1.547	1.570	1.563
120 (6,6)	0.591	0.563	0.803	0.840	1.638	1.659	1.660
140 (7,7)	0.561	0.534	0.802	0.840	1.689	1.708	1.716
160 (8,8)	0.536	0.511	0.804	0.841	1.714	1.725	1.745
180 (9,9)	0.514	0.491	0.805	0.841	1.713	1.726	1.744
200 (10,10)	0.497	0.474	0.805	0.841	1.712	1.724	1.744
∞ (∞,∞) extrapolation	0.415	0.397	0.810	0.844	1.713	1.725	1.744

[a] Molecular globularity.
[b] Reference: calculations carried out with the GEPOL program.
[c] Molecular rugosity (Å^{-1}).
[d] Fractal–like index of the solvent–accessible surface.
[e] Fractal–like index of the solvent–accessible surface averaged for non–buried atoms.

The topological indices for SWNTs (*cf.* Table 3) have been calculated with TOPO and GEPOL. The molecular globularity decreases ≈21% from $G_{(9,0)}$ to $G_{(18,0)}$ and from $G_{(5,5)}$ to $G_{(10,10)}$, being *G* the index that better differentiates among SWNTs. In particular both values of $G_{(10,10)}$ are minims. However, molecular rugosity *G'* is almost constant through Table 3.

The fractal–like index *D* of the solvent–accessible surface increases ≈9% through Table 3. The corresponding interpretation is that the solvent–accessible surface of thinner SWNTs is less sensitive to solvent size than that of thicker SWNTs. In particular D–$D'_{(10,10)}$ lie in the corresponding saturation lines. Figure 4 presents GEPOL fractal–like index $D_{(n,0)-(n,n)}$ *vs.* $(n^2+nm+m^2)^{1/2}$. In the whole range of $(n^2+nm+m^2)^{1/2}$, calculated $D_{(n,0)}$ is somewhat smaller than $D_{(n,n)}$. The initial slope of the (*n*,0) curve is slightly smaller than that of the (*n*,*n*) curve. For thicker

SWNTs, D shows saturation after $D_{(12,0)–(7,7)}$. $D_{(10,10)}$ corresponds to saturation for (n,n), which is greater than those for all $(n,0)$.
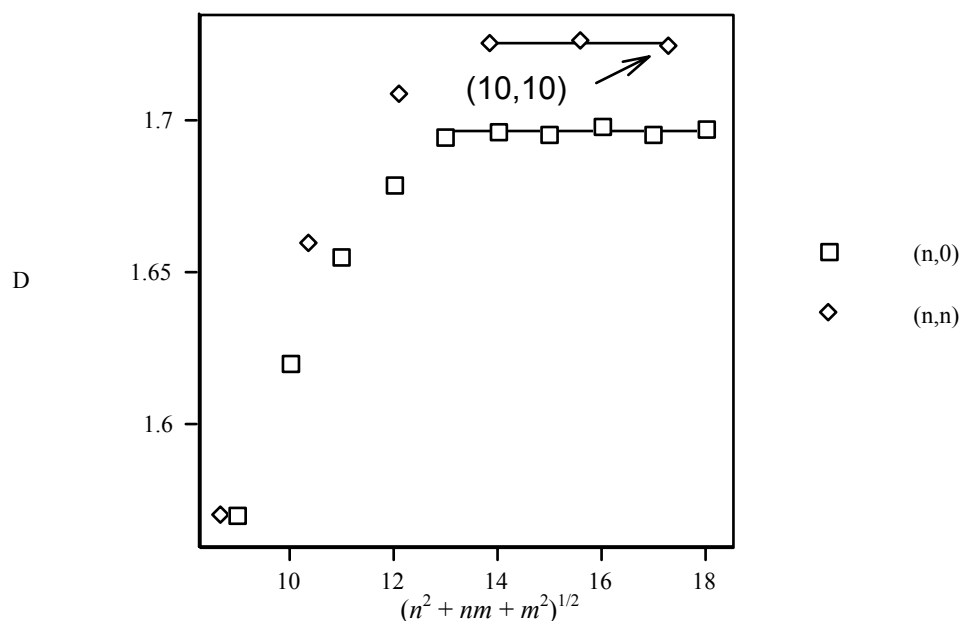
Figure 4. Variation of GEPOL fractal–like index D *vs.* $(n^2 + nm + m^2)^{1/2}$.

Table 4. Geometric Descriptors and Topological Indices for SWNTs. Analysis for an Ending Divalent C Atom

Nanotube	V^a	S^b	G^c	G'^d	AS^e	Accessibility ^{f}	AS'^g	D^h
90 (9,0)	11.5	14.25	1.730	1.239	23.42	21.42	43.33	1.402
100 (10,0)	11.5	14.19	1.739	1.231	23.53	21.51	41.82	1.444
110 (11,0)	11.4	14.62	1.679	1.279	23.70	21.67	41.20	1.468
120 (12,0)	11.5	14.20	1.735	1.235	23.67	21.65	41.00	1.469
130 (13,0)	11.5	14.29	1.725	1.242	23.84	21.80	40.63	1.487
140 (14,0)	11.5	14.40	1.709	1.255	23.90	21.86	40.51	1.486
150 (15,0)	11.5	14.20	1.737	1.232	23.57	21.56	40.53	1.471
160 (16,0)	11.5	14.51	1.696	1.265	23.88	21.84	40.60	1.479
170 (17,0)	11.4	14.61	1.680	1.277	23.85	21.81	40.40	1.485
180 (18,0)	11.5	14.49	1.697	1.264	24.09	22.02	40.60	1.485
∞ (∞,0) extrapolation	11.5	14.72	1.668	1.287	24.46	22.37	37.99	1.572
100 (5,5)	11.6	13.63	1.823	1.171	21.37	19.54	40.00	1.393
120 (6,6)	11.7	13.28	1.876	1.136	21.66	19.81	38.07	1.451
140 (7,7)	11.7	13.64	1.826	1.167	21.93	20.05	36.65	1.496
160 (8,8)	11.7	13.64	1.825	1.168	21.72	19.86	36.51	1.490
180 (9,9)	11.6	13.78	1.804	1.183	21.87	20.00	36.36	1.504
200 (10,10)	11.6	14.00	1.773	1.204	22.00	20.12	36.34	1.505
∞ (∞,∞) extrapolation	11.6	14.26	1.744	1.225	22.55	20.63	32.85	1.653

^{a} Atomic volume (Å^3)
^{b} Atomic surface area (Å^2)
^{c} Atomic globularity
^{d} Atomic rugosity (Å^{-1})
^{e} Atomic water–accessible surface area (Å^2)
^{f} Atomic accessibility (per cent) of the accessible surface
^{g} Atomic side–chain accessible surface area (Å^2)
^{h} Atomic fractal–like index of the solvent–accessible surface

The fractal–like index averaged for non–buried atoms D' increases $\approx$10% through Table 3. The comparison between $D_{(n,0)–(n,n)}$ and $D'_{(n,0)–(n,n)}$ shows that the difference $D' - D$ increases from $\approx$1% to $\approx$2% through Table 3, meaning that the central atoms in thinner SWNTs are essentially buried for most solvents, while those in thicker SWNTS are unlikely buried for different solvents, being more buried for solvents with greater molecular size.

The atomic analysis of the geometric descriptors and topological indices for SWNTs has been performed with TOPO (*cf.* Table 4). The atomic contribution of an ending divalent C atom to the molecular volume V is almost constant. However, its atomic component parts in the bare molecular surface area S and rugosity G' increase $\approx$2% through Table 4. By contrast, the atomic term in the molecular globularity G decreases $\approx$2% through Table 4. In turn, the parts in the water–accessible surface area AS and corresponding accessibility increase $\approx$3% through Table 4. The contribution to the side–chain accessible surface area AS' is the descriptor that better differentiates among SWNTs, decreasing $\approx$8% through Table 4. The term in the fractal–like index D increases $\approx$7% through Table 4. In particular V–S–G–G'–AS–accessibility$_{(10,10)}$ are similar to the corresponding optima near (18,0); AS'–$D_{(10,10)}$ are optima.

Table 5. Geometric Descriptors for Single–Wall Carbon Nanotube Fragments

Nanotube	V_{totl} [a]	V [b]	V_{cav}	ρ_{tot} [c]	S_{ext} [d]	S [b]	S_{cav}	AS_{ext} [e]	AS [b]	AS_c	AS'_{ext} [f]	AS' [b]	AS'_{cv}
90 (9,0)	>391	806	–	<2.042	365	686	321	632	823	191	1171	1279	108
100 (10,0)	>317	894	–	<2.041	307	761	454	576	919	343	1104	1364	260
110 (11,0)	1132	985	147	1.758	634	839	205	913	1009	96	1452	1450	0
120 (12,0)	1242	1074	168	1.748	670	915	245	983	1100	117	1541	1538	0
130 (13,0)	1390	1164	226	1.692	733	993	260	1057	1193	136	1631	1635	4
140 (14,0)	1559	1254	305	1.624	738	1070	332	1075	1286	211	1738	1757	19
150 (15,0)	1708	1343	365	1.588	812	1145	333	1161	1376	215	1827	1886	59
160 (16,0)	1860	1434	426	1.556	824	1223	399	1196	1470	274	1943	2009	66
170 (17,0)	2076	1523	553	1.481	885	1300	415	1257	1563	306	2031	2135	104
180 (18,0)	2238	1612	626	1.455	891	1377	486	1283	1655	372	2106	2260	154
100 (5,5)	>338	892	–	<2.048	316	748	432	621	877	256	1189	1357	168
120 (6,6)	>299	1072	–	<2.046	289	900	611	585	1049	464	1140	1502	362
140 (7,7)	>227	1250	–	<2.045	231	1050	819	513	1227	714	1041	1666	625
160 (8,8)	1776	1430	346	1.629	833	1202	369	1173	1404	231	1849	1857	8
180 (9,9)	2118	1609	509	1.537	935	1354	419	1292	1577	285	2029	2093	64
200 (10,10)	2435	1789	646	1.486	989	1504	515	1379	1762	383	2198	2333	135

[a] Fragment volume (Å^3)
[b] Reference: calculations carried out with the GEPOL program
[c] Fragment density (g·cm^{-3})
[d] Fragment surface area (Å^2)
[e] Fragment water–accessible surface area (Å^2)
[f] Fragment side–chain accessible surface area (Å^2)

The comparison between GEPOL and SURMO2 is of especial interest because the latter does not recognize the internal cavity of the SWNTs. However, the combination of GEPOL and SURMO2 allows analyzing the cavity. The cavity contributes to the total volume and molecular surface area of a SWNT. On the one hand, the total volume V_t for a SWNT is the sum of the molecular V_m and cavity V_c volumes: $V_t = V_m + V_c$. The geometric descriptors of SWNTs with their

cavities have been calculated with SURMO2 (*cf.* Table 5). SURMO2 is unable to recognize the cavities and measures the total volume, which, *e.g.*, results $V_{t(11,0)} = 1132\text{Å}^3$. Furthermore, GEPOL recognizes the cavity and the molecular volume results $V_{m(11,0)} = 985\text{Å}^3$. On the other hand, the molecular surface area S_m is the sum of the external S_e and cavity S_c surface areas: $S_m = S_e + S_c$. The correct external surface area $S_{e(11,0)} = 634\text{Å}^2$ (SURMO2). Moreover, the actual (external plus internal) molecular surface area $S_{m(11,0)} = 839\text{Å}^2$ (GEPOL). From the calculation results referring to the total (SURMO2) and cavity–sensitive (GEPOL) molecular shape, the geometric descriptors V_c and S_c have been estimated for SWNT cavities. The results for thicker SWNTs show that $S_{cav} > AS_{cav} >> AS'_{cav}$, meaning that although many water molecules with $R_{effective} = 1.41\text{Å}$ and $V \approx 12\text{Å}^3$ can, in principle, be contained inside a SWNT, the lengthened form of the cavity provides little continuous space available for whole water molecules. Furthermore, probe spheres representing protein side chains with $R_{eff} = 3.5\text{Å}$ ($V \approx 180\text{Å}^3$) cannot be easily contained in the cavity because continuous space enough is hardly available. This effect is more marked for SWNTs of intermediate diameter. In particular the three volumes for (10,10) are maxims.
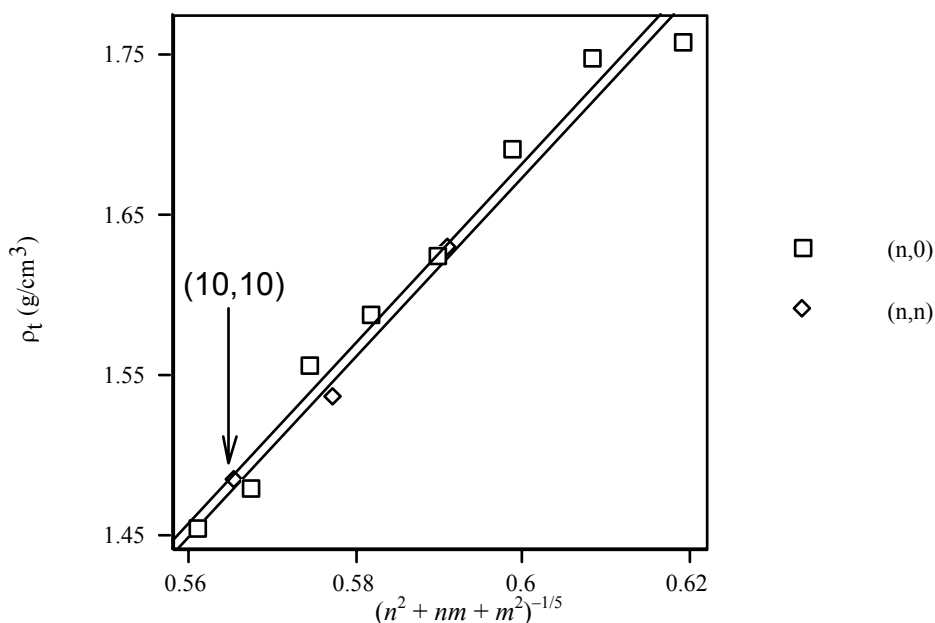
Figure 5. Variation of SURMO2 density ρ_t *vs.* $(n^2 + nm + m^2)^{-1/5}$.

The density of SWNTs, ρ_t calculated from SURMO2 V_t with cylinder packing density $\eta = \pi/[2(3)^{1/2}] \approx 0.907$, decreases $\approx 17\%$ through Table 5, meaning that thicker SWNTs include greater cavities, which are not accessible to other equal SWNTs. In particular $\rho_{t(10,10)}$ is similar to the minimum $\rho_{t(18,0)}$. Figure 5 presents the densities $\rho_{t(n,0)-(n,n)}$ *vs.* $(n^2+nm+m^2)^{-1/5}$. ρ_t of thinner SWNTs is greater than that of thicker SWNTs. Both representations correlate well with $(n^2+nm+m^2)^{-1/5}$. The variation of $\rho_{t(n,0)}$ with $(n^2+nm+m^2)^{-1/5}$ is:

$$\rho_{t(n,0)} = -1.67 + 5.58\left(n^2 + nm + m^2\right)^{-1/5} \quad N = 8 \quad r = 0.987 \quad s = 0.020 \quad F = 224.2 \tag{20}$$

The variation of $\rho_{t(n,n)}$ with $(n^2+nm+m^2)^{-1/5}$ is:

$$\rho_{t(n,n)} = -1.67 + 5.57\left(n^2 + nm + m^2\right)^{-1/5} \tag{21}$$

$\rho_{t(10,10)}$ is slightly greater than $\rho_{t(17,0)}$, and rather greater than $\rho_{t(18,0)}$ and than those extrapolated for $\rho_{t(19-20,0)}$.

Table 6. *s* Ratio in the sp^n Hybrid Orbitals and Density for Various Forms of Carbon

Form of carbon	Bond angle [a]	s ratio [b]	ρ_{total} [c]
glassy carbon SPI–Glas 25	–	–	1.420
(18,0)	119.7	33.2	1.455 [d]
(17,0)	119.7	33.1	1.481 [d]
(10,10)	119.7	33.2	1.486 [d]
(9,9)	119.7	33.1	1.537 [d]
glassy carbon SPI–Glas 10	–	–	1.540
(16,0)	119.7	33.1	1.556 [d]
(15,0)	119.6	33.1	1.588 [d]
(14,0)	119.6	33.1	1.624 [d]
(8,8)	119.6	33.0	1.629 [d]
graphite AGKSP	120.0	33.3	1.630
fullerite (C$_{60}$)–film	116.0	30.5	1.670
(13,0)	119.5	33.0	1.692 [d]
(12,0)	119.4	33.0	1.748 [d]
fullerite (C$_{60}$)	116.0	30.5	1.750
(11,0)	119.3	32.9	1.758 [d]
graphite UF–4S	120.0	33.3	1.760
graphite SPK	120.0	33.3	1.800
amorphous carbon	–	–	1.800–2.100
hollow graphite nanofiber (*ca.* 8 layers)	–	–	2.000
graphite	120.0	33.3	2.260
diamond	109.5	25.0	3.513

[a] Bond angle averaged for trivalent atoms (º)
[b] s ratio in the sp^n hybrid orbitals (per cent)
[c] Density (g·cm^{-3})
[d] Calculations carried out with the SURMO2 program

SURMO2 density ρ_t for SWNTs and experimental density for other forms of carbon are summarized in Table 6. The great decrease in bond angle ϕ from graphite $\phi = 120.0º$ to diamond $\phi = 109.5º$, interpreted by the change of sp^n hybrid orbitals from sp^{2-3}, can explain the increase in density from $\rho_t = 2.260$ to 3.513g·cm^{-3}. However, the smaller decrease in ϕ from graphite $\phi = 120.0º$ to SWNTs $\phi \approx 119.5º$ to fullerite $\phi = 116.0º$, interpreted by the decrease in s ratio $[\cos\phi = -s/(1-s)]$ from 33.3–33.0–30.5% in sp^n hybrid orbitals from $sp^{2.000-2.031-2.281}$, cannot explain the decrease in density from $\rho_t = 2.260$ to ≈ 1.7–1.750g·cm^{-3}. The drastic change in density among the various forms of carbon is a consequence of the crystalline structure that each substance adopted. The macroscopically measured density is usually slightly different than that measured using X–ray diffraction because of defects and/or impurities within the sample. Furthermore, most graphites exhibit considerable porosity whereas thicker SWNTs and glassy carbons are quite dense, certainly much more so than graphite. This might sound like a contradiction, but when one looks at

the density of thicker SWNTs and glassy carbons in comparison to the theoretical density of the graphite crystal, their density is less, specifically $\approx$1.5 *vs*. 2.260g·cm^{-3}. However, since graphite normally has considerable porosity, the $\approx$1.5g·cm^{-3} density is higher than that of the typical graphite. On the other hand, the density of thinner SWNTs is *ca*. that of fullerite ρ_t = 1.750g·cm^{-3}. In general the density of SWNTs is *ca*. one sixth that of steel ρ_t = 7.753g·cm^{-3}.

Table 7. Topological Indices for Single–Wall Carbon Nanotube Fragments

Nanotube	G_{ext} [a]	G_{mol} [b]	G_{cav}	G'_{ext} [c]	G'_{mol} [b]	G'_{cav}	D_{ext} [d]	D_{mol} [b]	D_{cav}
90 (9,0)	0.708–1.000	0.611	–	<0.934	0.851	–	1.402	1.570	2.546
100 (10,0)	0.732–1.000	0.590	–	<0.968	0.851	–	1.369	1.620	2.278
110 (11,0)	1.000	0.570	0.657	0.439	0.852	1.395	1.553	1.655	6.762
120 (12,0)	0.834	0.554	0.601	0.539	0.852	1.458	1.570	1.679	3.641
130 (13,0)	0.821	0.539	0.690	0.528	0.853	1.150	1.584	1.694	4.960
140 (14,0)	0.881	0.526	0.660	0.474	0.853	1.089	1.533	1.696	4.582
150 (15,0)	0.851	0.514	0.742	0.476	0.853	0.912	1.555	1.695	3.287
160 (16,0)	0.888	0.503	0.686	0.443	0.853	0.937	1.527	1.698	3.355
170 (17,0)	0.889	0.492	0.785	0.427	0.853	0.751	1.533	1.695	2.986
180 (18,0)	0.929	0.483	0.728	0.398	0.854	0.776	1.518	1.697	2.818
∞ (∞,0) extrapolation	1.000	0.404	1.000	0.343	0.856	0.431	1.747	1.860	2.000
100 (5,5)	0.743–1.000	0.599	–	<0.935	0.838	–	1.372	1.570	2.380
120 (6,6)	0.749–1.000	0.563	–	<0.965	0.840	–	1.353	1.659	2.259
140 (7,7)	0.780–1.000	0.534	–	<1.015	0.840	–	1.315	1.708	2.134
160 (8,8)	0.851	0.511	0.646	0.469	0.841	1.067	1.557	1.725	4.876
180 (9,9)	0.853	0.491	0.736	0.441	0.841	0.823	1.562	1.726	3.370
200 (10,10)	0.885	0.474	0.702	0.406	0.841	0.797	1.547	1.724	2.942
∞ (∞,∞) extrapolation	1.000	0.397	1.000	0.266	0.844	0.386	1.863	1.947	2.000

[a] Fragment globularity
[b] Reference: calculations carried out with the GEPOL program
[c] Fragment rugosity (Å^{-1})
[d] Fragment fractal–like index of the solvent–accessible surface
[e] Fragment fractal–like index of the solvent–accessible surface averaged for non–buried atoms

The topological indices for SWNT fragments are indicated in Table 7. The molecular globularity G increases in the order: $G_{mol} < G_{cav} < G_{ext}$. In particular the three $G_{(10,10)}$ are similar to the optima near (18,0). By contrast, the molecular rugosity G' for thicker SWNTs varies in the opposite direction: $G'_{ext} < G'_{cav} < G'_{mol}$. The three $G'_{(10,10)}$ are similar to the optima near (18,0).

The internal cavity shows the greatest fractal–like index $D_{ext} < D_{mol} << D_{cav}$ (*cf*. Table 7), indicating that its solvent–accessible surface is the most sensitive to solvent size. Therefore, it is suggested that the catalytic activity of a SWNT could be located in the internal cavity, being (11,0) the cavity with maximum D_{cav}. The cavities of thicker SWNTs as (18,0)–(10,10) show smaller D_{cav}. D_{cav} = 2 is expected for the planar graphene sheet. In particular the three $D_{(10,10)}$ are similar to the optima near (18,0). Figure 6 exhibits SURMO2/GEPOL fractal–like index of the cavity $D_{cav(n,0)-(n,n)}$ *vs*. $(n^2+nm+m^2)^{1/2}$. For the thickest and thinnest SWNTs, $D_{cav(n,0)-(n,n)} \sim 2$. The $(n,0)$ curve shows a discontinuity in D_{cav} for $(n^2+nm+m^2)^{1/2}$ in the range from 11–14. The (n,n) curve presents this discontinuity at $(n^2+nm+m^2)^{1/2} \approx 14$. In this $(n^2+nm+m^2)^{1/2}$ range $D_{cav(n,0)}$ is, in general, greater than $D_{cav(n,n)}$. For thicker SWNTs, $D_{cav(n,0)-(n,n)}$ extrapolate to 2. Among SWNTs (10,10) is special

presenting a relatively great D (*cf.* Figure 4) and small D_{cav}.
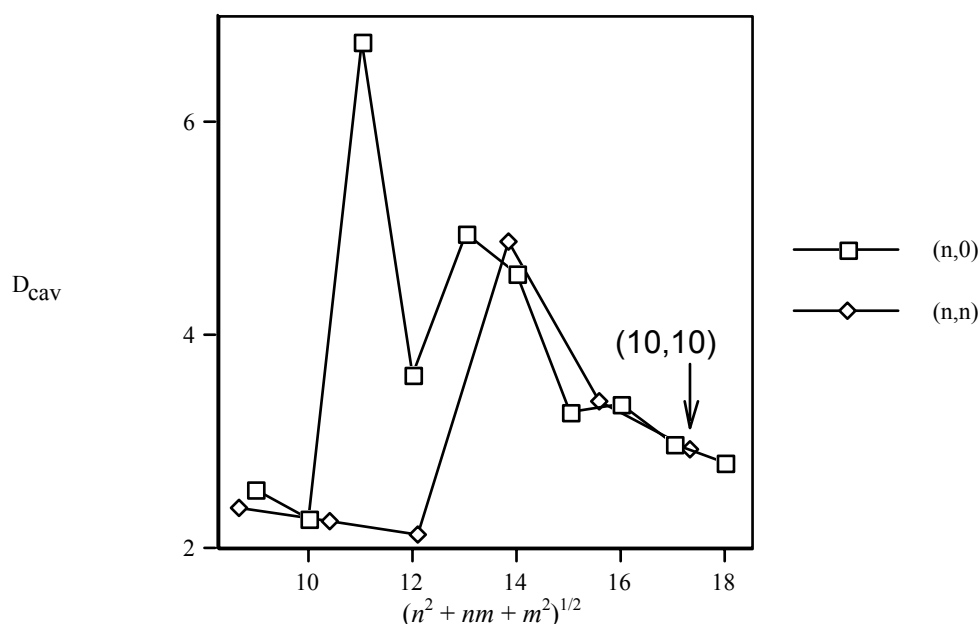
Figure 6. Variation of the fractal–like index of the cavity D_{cav} *vs.* $(n^2 + nm + m^2)^{1/2}$.

Table 8. Solubility, Free Energy of Solvation and Partition Coefficient Results for Single–Wall Carbon Nanotubes

Nanotube	log S_w [a]	$\Delta G_{sol,w}$ [b]	$\Delta G_{sol,o}$ [c]	$\Delta G_{sol,ch}$ [d]	$\Delta G_{sol,cf}$ [e]	log P_o [f]	log P_o Ref. [g]	log P_{ch} [h]	log P_{ch} Ref. [i]	log P_{cf} [j]	log P_{cf} Ref. [i]
90 (9,0)	−36.6	−25.3	−195.1	−105.2	−160.2	29.8	23.7	14.1	18.3	23.7	32.3
100 (10,0)	−40.1	−28.3	−222.0	−118.2	−179.8	34.0	28.0	15.8	21.1	26.6	37.0
110 (11,0)	−43.6	−31.3	−247.3	−131.3	−199.1	37.9	29.1	17.6	23.8	29.5	41.4
120 (12,0)	−47.1	−34.3	−271.7	−144.0	−218.0	41.7	33.0	19.3	26.3	32.3	45.6
130 (13,0)	−50.7	−37.3	−295.7	−156.7	−237.0	45.4	34.4	21.0	28.8	35.1	49.8
140 (14,0)	−54.2	−40.3	−319.5	−169.1	−256.2	49.1	38.1	22.6	31.3	37.9	53.9
150 (15,0)	−57.7	−43.2	−343.2	−181.6	−274.8	52.7	39.7	24.3	33.7	40.7	58.0
160 (16,0)	−61.3	−46.1	−366.8	−194.1	−293.6	56.3	43.3	26.0	36.2	43.5	62.1
170 (17,0)	−64.8	−48.9	−389.3	−207.0	−312.2	59.8	45.0	27.8	38.5	46.2	66.0
180 (18,0)	−68.4	−52.0	−413.8	−218.7	−330.6	63.6	48.5	29.3	41.1	48.9	70.2
100 (5,5)	−40.7	−27.5	−211.3	−114.8	−174.4	32.3	25.8	15.3	20.0	25.8	35.0
120 (6,6)	−47.8	−33.5	−264.0	−140.8	−212.6	40.5	31.0	18.8	25.5	31.5	44.2
140 (7,7)	−54.8	−39.5	−313.1	−165.7	−251.1	48.1	36.2	22.2	30.6	37.2	52.8
160 (8,8)	−61.9	−45.2	−359.8	−190.4	−288.2	55.3	41.6	25.5	35.5	42.7	60.9
180 (9,9)	−69.0	−51.0	−406.9	−215.0	−325.2	62.5	46.7	28.8	40.4	48.2	69.1
200 (10,10)	−76.1	−56.8	−453.3	−239.5	−362.1	69.6	51.9	32.1	45.2	53.6	77.1

[a] S_w is the solubility in water (mol·L^{-1})
[b] Gibbs free energy of solvation in water (kJ·mol^{-1})
[c] Gibbs free energy of solvation in 1–octanol (kJ·mol^{-1})
[d] Gibbs free energy of solvation in cyclohexane (kJ·mol^{-1})
[e] Gibbs free energy of solvation in chloroform (kJ·mol^{-1})
[f] P_o is the 1–octanol–water partition coefficient
[g] Calculations carried out with a method by Kantola *et al.*
[h] P_{ch} is the cyclohexane–water partition coefficient
[i] Calculations carried out with a method by Leo and Hansch
[j] P_{cf} is the chloroform–water partition coefficient

The aqueous solubility S_w for SWNTs has been calculated with our program based on the AQUAFAC model [41] (*cf*. Table 8). AQUAFAC S_w decreases monotonically with *n* and *m*. All the values of $\log S_w < -3$, meaning that less than 0.1% of SWNT is in solution. Even all the minus $\log S_w$ values are greater than the Avogadro number exponent 23, $S_w < 10^{-23}$, meaning that no solute molecule would be present in solution to allow experiments for validation. However, all the $\log S_w$ figures are kept with the only purpose of comparison along the series. The results are consistent with the fact that SWNTs are completely insoluble in water [42]. The solubility of SWNTs is hindered because SWNTs aggregate in bundles due to large van der Waals interactions. Although individual van der Waals forces are weak, the total force is large because of the great number of atoms interacting between the surfaces of aligned SWNTs. Therefore, SWNTs are difficult to dissolve or suspend. Ways of increasing the solubility of SWNTs include the use of anionic surfactants, *e.g.*, sodium dodecylsulphate (SDS), nonionic surfactants, *e.g.*, Triton X–100, chemical modification or polymer wrapping SWNTs. In particular $S_{w(10,0)}$ is minimum. Figure 7 reveals the logarithm of AQUAFAC solubility in water, $\log S_{w(n,0)-(n,n)}$ *vs*. $(n^2+nm+m^2)^{1/2}$. Both representations correlate well with $(n^2+nm+m^2)^{1/2}$. The absolute value of the slope for the (*n*,0) curve is smaller than that for the (*n*,*n*) curve. Calculated $\log S_{w(n,0)}$ is greater than $\log S_{w(n,n)}$, especially for thicker SWNTs. The variation of $\log S_{w(n,0)}$ with $(n^2+nm+m^2)^{1/2}$ is:

$$\log S_{w(n,0)} = -4.76 - 3.53\left(n^2 + nm + m^2\right)^{1/2} \tag{22}$$
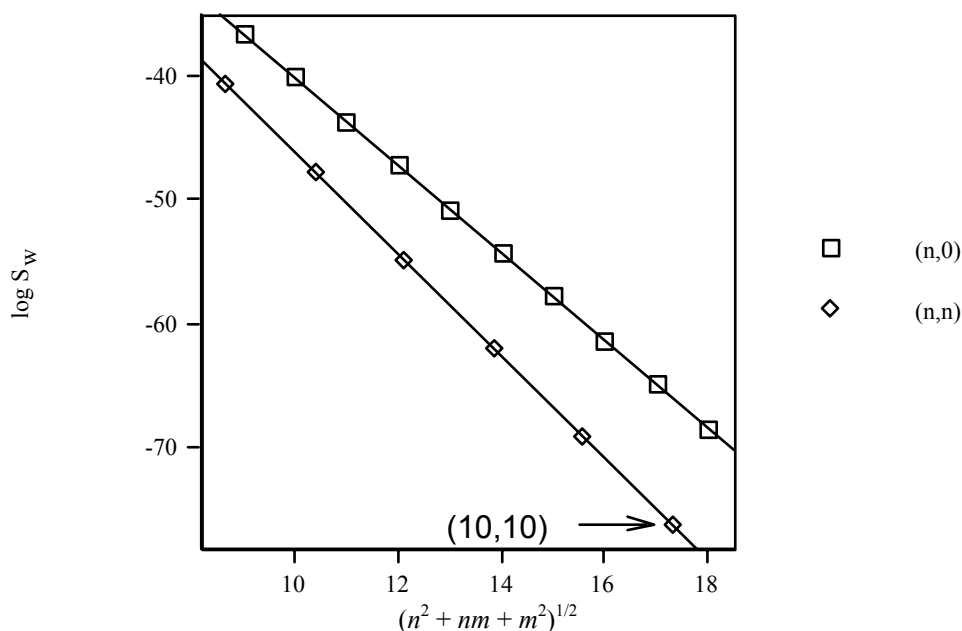
Figure 7. Variation of AQUAFAC logarithm of solubility in water *vs*. $(n^2 + nm + m^2)^{1/2}$.

However, AQUAFAC is valid only for small SWNTs, and the correlations between computed properties and SWNT parameters are, therefore, exaggerated. The same happens for the three partition coefficients in Figure 8. The variation of $\log S_{w(n,n)}$ with $(n^2+nm+m^2)^{1/2}$ is:

$$\log S_{\text{w}(n,n)} = -5.31 - 4.09\left(n^2 + nm + m^2\right)^{1/2} \tag{23}$$

Log$S_{\text{w}(10,10)}$ is the smallest for all SWNTs.

The free energies of solvation and partition coefficients (*cf.* Table 8) have been calculated with our program SCAP [43]. The 1–octanol–water partition coefficients logP_o have been compared with values calculated with our program CDHI, which is based on a method developed by Kantola *et al.* [44]. SCAP P_o increases monotonically with *n* and *m*. All the values of log$P_\text{o} > 3$, meaning that more than 99.9% of the solute is in the organic phase, and a negligible quantity of solute is predicted in the aqueous phase. Even all the logP_o values are greater than the Avogadro exponent, and no solute molecule would be present in the aqueous phase to allow experiments. P_o results are of the same order of magnitude as CDHI computations. LogP_o relative error is 30%. In particular log$P_{\text{o}(10,10)}$ is maximum. Figure 8 illustrates SCAP log$P_{\text{o}(n,0)}$ and log$P_{\text{o}(n,n)}$ *vs.* $(n^2+nm+m^2)^{1/2}$. Both representations correlate well with $(n^2+nm+m^2)^{1/2}$. The slope for the (*n*,0) curve is slightly smaller than that of the (*n*,*n*) curve. Calculated log$P_{\text{o}(n,0)}$ is smaller than log$P_{\text{o}(n,n)}$, especially for thicker SWNTs. The variation of log$P_{\text{o}(n,0)}$ with $(n^2+nm+m^2)^{1/2}$ is:

$$\log P_{\text{o}(n,0)} = -3.17 + 3.72\left(n^2 + nm + m^2\right)^{1/2} \tag{24}$$

However, SCAP is valid only for small SWNTs, and the correlations between computed properties and SWNT parameters are exaggerated. The variation of log$P_{\text{o}(n,n)}$ with $(n^2+nm+m^2)^{1/2}$ is:

$$\log P_{\text{o}(n,n)} = -4.27 + 4.28\left(n^2 + nm + m^2\right)^{1/2} \tag{25}$$

Cyclohexane– and chloroform–water partition coefficients, $P_{\text{ch–cf}}$, increase monotonically with *n* and *m* (*cf.* Table 8). In order to compare our results, the method proposed by Leo and Hansch has been used [45]. Most log*P* values are greater than the Avogadro exponent, and no solute molecule would be present in the aqueous phase to allow experiments. $P_{\text{ch–cf}}$ results are of the same order of magnitude as calculations performed with the method by Leo and Hansch. Log$P_{\text{ch–cf}}$ relative errors are –27% and –29%, respectively. Log$P_{\text{ch–cf}(10,10)}$ are maxims. The variation of log$P_{\text{ch}(n,0)}$ with $(n^2+nm+m^2)^{1/2}$ (*cf.* Figure 8) is:

$$\log P_{\text{ch}(n,0)} = -1.08 + 1.69\left(n^2 + nm + m^2\right)^{1/2} \tag{26}$$

The variation of log$P_{\text{ch}(n,n)}$ with $(n^2+nm+m^2)^{1/2}$ is:

$$\log P_{\text{ch}(n,n)} = -1.35 + 1.93\left(n^2 + nm + m^2\right)^{1/2} \tag{27}$$

The variation of log$P_{\text{cf}(n,0)}$ with $(n^2+nm+m^2)^{1/2}$ is:

$$\log P_{\text{cf}(n,0)} = -1.36 + 2.80\left(n^2 + nm + m^2\right)^{1/2} \tag{28}$$

The variation of log$P_{\text{cf}(n,n)}$ with $(n^2+nm+m^2)^{1/2}$ is:

$$\log P_{\text{cf}(n,n)} = -1.87 + 3.21\left(n^2 + nm + m^2\right)^{1/2} \tag{29}$$

Log$P_{\text{o–ch–cf(10,10)}}$ are the greatest for all SWNTs.
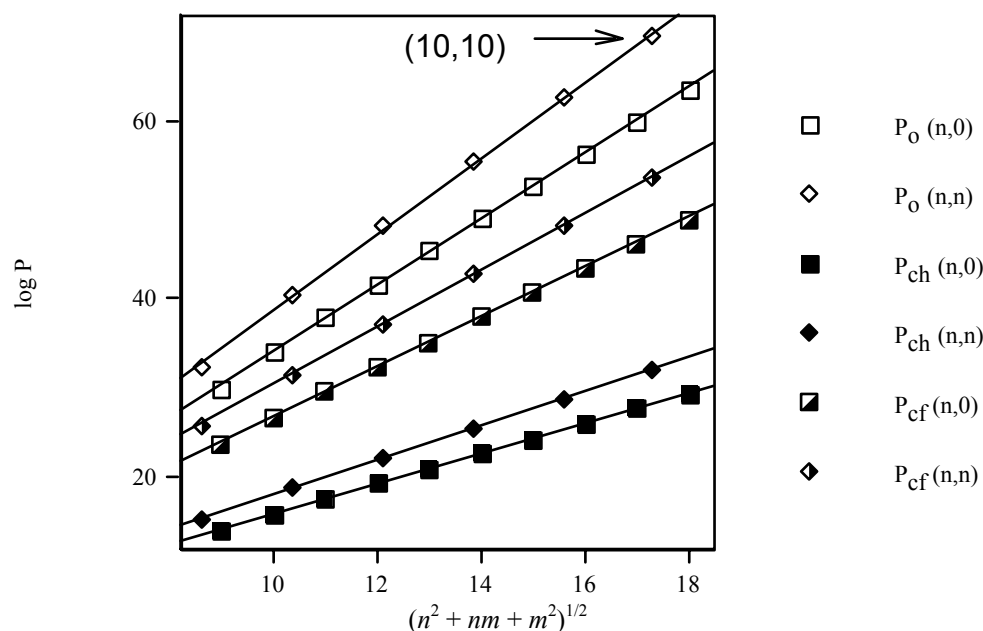
Figure 8. Variation of SCAP logarithm of organic solvent–water partition coefficient *vs.* $(n^2 + nm + m^2)^{1/2}$.

Table 9. Permittivity, Ionization Potential, Electron Affinity, Volume and Charge Transfer for Different Solvents

Solvent/suspender	$\varepsilon^{\,a}$	$I^{\,b}$	$EA^{\,c}$	$V^{\,d}$	Charge transfer
n–hexane	1.890	1002.7	–290.9	103.5	SWNT$^-$/solvent$^+$
carbon disulphide	2.641	864.4	129.2	55.5	SWNT$^+$/solvent$^-$
1–methylnaphthalene	2.710	778.0	73.5	146.9	SWNT$^+$/solvent$^-$
chloroform (CHCl$_3$)	4.806	1084.8	108.1	72.1	SWNT$^+$/solvent$^-$
ortho–dichlorobenzene (ODCB)	$9.930^{\,e}$	$854.9^{\,f}$	71.5	110.3	SWNT$^+$/solvent$^-$
water	80.37	1150.2	–332.3	23.8	SWNT$^-$/solvent$^+$

[a] Relative dielectric permittivity at 20ºC
[b] Ionization potential (kJ·mol^{-1}) calculated with MOPAC–AM1
[c] Electron affinity (kJ·mol^{-1}) calculated with MOPAC–AM1
[d] Molecular volume (Å^3)
[e] At 25ºC
[f] Calculated with MOPAC–MNDO–d

Although the solubility in the organic solvents is predicted rather greater than in water log$P \gg 1$, the absolute solubility in organic solvents is also estimated extremely small, *e.g.*, $S_{\text{cf(10,10)}} \approx P_{\text{cf}} \cdot S_w = 10^{53.6} \cdot 10^{-76.1} = 10^{-22.5}$ mol·L^{-1}. The results are consistent with the experimental observation that there are rather few good solvents for SWNTs, if any [46,47]. Toluene, ethanol, isopropyl alcohol, acetone and similar solvents do not work. However, chloroform (CHCl$_3$) keeps SWNTs in more or less stable suspension for days. It is suggested that most other chlorinated solvents, *e.g.*, *ortho*–dichlorobenzene (ODCB) behave similarly. The relative dielectric permittivity ε, MOPAC–AM1 ionization potential (*I*), electron affinity (EA), TOPO molecular volume *V* and charge transfer for different solvents are listed in Table 9. CHCl$_3$ and ODCB have similar dielectric permittivities and EAs, and suspend SWNTs. Other solvents that are co–miscible with ODCB but

that are a poor ε–EA match, such as *n*–hexane, do not dissolve/suspend SWNTs. The results are in agreement with electroplating experiments that showed that SWNTs in ODCB and ODCB–CHCl$_3$ are positively charged [48]. However, SWNTs are not suspended in ODCB–*n*–hexane. These observations are attributed to the large EA of ODCB and the negative EA of *n*–hexane. It is suggested that SWNTs in CHCl$_3$ are positively charged due to the large positive EA of CHCl$_3$, and that SWNTs in other chlorinated solvents with large positive EA are also positively charged. By contrast, when SWNTs are suspended using certain nonionic surfactants, *e.g.*, Triton X, colloids of negatively charged SWNTs are produced. Controllable aggregation of SWNTs is achieved diluting a SWNT–ODCB solution with CHCl$_3$. Greater aggregation (diluting SWNT–ODCB with *n*–hexane) causes complete precipitation of SWNTs.

4 CONCLUSIONS

The following conclusions can be made from this study.

1. The calculated elementary polarizability relationships of any SWNT (*n*,*m*) is similar to that of its neighbor (*n*–1,*m*+1). The trend is approximately repeated for each period. (9,0) and (5,5), which join smoothly to a C$_{60}$ hemisphere, are the smallest diameter SWNTs that can be properly capped.

2. The observed correlations between $(n^2+nm+m^2)^{1/2}$, $<\alpha>$, d_t, ρ_l, θ, D, ρ_t, logS_w, logP_o, logP_{ch} and logP_{cf} show that the (*n*,*m*) indices, which have been used to built the PT are adequate. The most interesting index combination is $(n^2+nm+m^2)^{1/2}$.

3. (10,10) is the favorite SWNT. (10,10) presents a relatively small $<\alpha>$, great d_t, great ρ_l, small θ, great D, great ρ_t, small D_{cav}, small S_w, great P_o, great P_{ch}, great P_{cf} and great kinetic stability.

4. SWNTs in some organic solvents are positively charged, while in water/Triton X are negatively charged. An explanation is given on the basis of ε and EA.

Work is in progress on the characterization of fullerenes, SWNTS, solvents and co–solvents such as Triton X–100, crown ethers, ethylenediaminetetraacetic acid, SDS, amylose–iodine–iodide complex, cyclopyranoses and lysozyme.

5 REFERENCES

[1]   Mendeleev, *The Principles of Chemistry*, Longmans and Green, London, 1905.
[2]   P. Pyykkö, Relativistic Effects in Structural Chemistry, *Chem. Rev.* **1988**, *88*, 563–594.
[3]   M. Randić and C. L. Wilkins, Graph Theoretical Ordering of Structures as a Basis for Systematic Searches for Regularities in Molecular Data, *J. Phys. Chem.* **1979**, *83*, 1525–1540.

[4]   M. Randić and C. L. Wilkins, Graph–Theoretical Analysis of Molecular Properties. Isomeric Variations in Nonanes, *Int*. *J*. *Quantum Chem*. **1980**, *18*, 1005–1027.

[5]   L. Bytautas and D. J. Klein, Formula Periodic Table for the Isomer Classes of Acyclic Hydrocarbons – Enumerative and Asymptotic Characteristics, *Croat*. *Chem*. *Acta* **2000**, *73*, 331–357.

[6]   L. Bytautas, D. J. Klein, and T. G. Schmalz, All Acyclic Hydrocarbons: Formula Periodic Table and Property Overlap Plots *via* Chemical Combinatorics, *New J*. *Chem*. **2000**, *24*, 329–336.

[7]   J. R. Dias, A Periodic Table for Polycyclic Aromatic Hydrocarbons, *Acc*. *Chem*. *Res*. **1985**, *18*, 241–248.

[8]   J. R. Dias, A Formula Periodic Table for Benzenoid Hydrocarbons and the Aufbau and Excised Internal Structure Concepts in Benzenoid Enumerations, *J*. *Math*. *Chem*. **1990**, *4*, 17–29.

[9]   D. J. Klein and W. A. Seitz, Pauling–Wheland Resonance Theory of Benzenoid Hydrocarbons, *J*. *Mol*. *Struct*. (*Theochem*) **1988**, *169*, 167–181.

[10] X. Liu, D. J. Klein, T. G. Schmalz, and W. A. Seitz, Generation of Carbon–Cage Polyhedra, *J*. *Comput*. *Chem*. **1991**, *12*, 1252–1259.

[11] X. Liu, D. J. Klein, W. A. Seitz, and T. G. Schmalz, Sixty–Atom Carbon Cages, *J*. *Comput*. *Chem*. **1991**, *12*, 1265–1269.

[12] A. T. Balaban, Theoretical Examination of New Forms of Carbon Formed by Intra– or Intermolecular Dehydrogenation of Polycyclic Aromatic Hydrocarbons, Particularly Helicenes, *Polycycl*. *Arom*. *Compounds* **2003**, *23*, 277–296.

[13] J. P. Corriou, O. Iordache, and D. Tondeur, Classification of Biomolecules by Information Entropy, *J*. *Chim*. *Phys*. *Phys*.–*Chim*. *Biol*. **1991**, *88*, 2645–2652.

[14] E. G. Gamaly and T. W. Ebbesen, Mechanism of Carbon Nanotube Formation in the Arc Discharge, *Phys*. *Rev*. *B* **1995**, *52*, 2083–2089.

[15] H. W. Kroto, J. R. Heath, S. C. O'Brien, R. F. Curl, and R. E. Smalley, C_{60}: Buckminsterfullerene, *Nature* (*London*) **1985**, *318*, 162–163.

[16] W. Krätschmer, L. D. Lamb, K. Fostiropoulos, and D. R. Huffman, Solid C_{60}: A New Form of Carbon, *Nature* (*London*) **1990**, *347*, 354–358.

[17] E. A. Rohlfing, D. M. Cox, and A. Kaldor, Production and Characterization of Supersonic Carbon Cluster Beams, *J*. *Chem*. *Phys*. **1984**, *81*, 3322–3330.

[18] E. G. Gamaly and L. T. Chadderton, Fullerene Genesis by Ion Beams, *Proc*. *R*. *Soc*. *London*, *A* **1995**, *449*, 381–409.

[19] L. T. Chadderton and E. G. Gamaly, *Nucl*. *Instrum*. *Meth*., *Sect*. *B* **1995**, *117*, 375.

[20] L. T. Chadderton and Y. Chen, Nanotube Growth by Surface Diffusion, *Phys*. *Lett*. *A* **1999**, *263*, 401–405.

[21] A. Thess, R. Lee, P. Nikolaev, H. Dai, P. Petit, J. Robert, C. Xu, Y. H. Lee, S. G. Kim, A. G. Rinzler, D. T. Colbert, G. E. Scuseria, D. Tománek, J. E. Fischer, and R. E. Smalley, Crystalline Ropes of Metallic Carbon Nanotubes, *Science* **1996**, *273*, 483–487.

[22] X. Zhao, Y. Liu, S. Inoue, T. Suzuki, R. O. Jones, and Y. Ando, Smallest Carbon Nanotube Is 3 Å in Diameter, *Phys*. *Rev*. *Lett*. **2004**, *92*, 125502–1–3.

[23] F. Torrens, Table of Periodic Properties of the Fullerenes Based on Structural Parameters, *J*. *Chem*. *Inf*. *Comput*. *Sci*. **2004**, *44*, 60–67.

[24] F. Torrens, Table of Periodic Properties of Fullerenes Based on Structural Parameters, *J*. *Mol*. *Struct*. (*Theochem*), in press.

[25] F. Torrens, Periodic Table of Carbon Nanotubes Based on the Chiral Vector, *Internet Electron*. *J*. *Mol*. *Des*. **2004**, *3*, 514–527, http://www.biochempress.com.

[26] F. Torrens, E. Ortí, and J. Sánchez–Marín, Vectorized TOPO Program for the Theoretical Simulation of Molecular Shape, *J*. *Chim*. *Phys*. *Phys*.–*Chim*. *Biol*. **1991**, *88*, 2435–2441.

[27] A. Bondi, Van der Waals Volumes and Radii, *J*. *Phys*. *Chem*. **1964**, *68*, 441–451.

[28] A. Y. Meyer, Molecular Mechanics and Molecular Shape. Part 1. Van der Waals Descriptors of Simple Molecules, *J*. *Chem*. *Soc*., *Perkin Trans*. *2*, **1985**, 1161–1169.

[29] R. B. Hermann, Theory of Hydrophobic Bonding. II. The Correlation of Hydrocarbon Solubility in Water with Solvent Cavity Surface Area, *J*. *Phys*. *Chem*., **1972**, *76*, 2754–2759.

[30] F. Torrens, J. Sánchez–Marín, and I. Nebot–Gil, New Dimension Indices for the Characterization of the Solvent–Accessible Surface, *J*. *Comput*. *Chem*. **2001**, *22*, 477–487.

[31] M. Lewis and D. C. Rees, Fractal Surfaces of Proteins, *Science* **1985**, *230*, 1163–1165.

[32] F. Torrens, J. Sánchez–Marín, and I. Nebot–Gil, AMYR 2: A New Version of a Computer Program for Pair Potential Calculation of Molecular Associations, *Comput. Phys. Commun.* **1998**, *115*, 87–89.

[33] B. Terryn and J. Barriol, On the Evaluation of the Usual Quantities or Coefficients Related to the Shape of a Molecule Approximated on the Basis of the van der Waals Radii, *J. Chim. Phys. Phys.–Chim. Biol.* **1981**, *78*, 207–212.

[34] J. L. Pascual–Ahuir, E. Silla, J. Tomasi, and R. Bonaccorsi, Electrostatic Interaction of a Solute with a Continuum. Improved Description of the Cavity and of the Surface Cavity Bound Charge Distribution, *J. Comput. Chem.* **1987**, *8*, 778–787.

[35] C. Voisin and A. Cartier, Determination of Distributed Polarizabilities to Be Used for Peptide Modeling, *J. Mol. Struct.* (*Theochem*) **1993**, *286*, 35–45.

[36] F. Torrens, Effect of Elliptical Deformation on Molecular Polarizabilities of Model Carbon Nanotubes from Atomic Increments, *J. Nanosci. Nanotech.* **2003**, *3*, 313–318.

[37] F. Torrens, Effect of Size and Deformation on Polarizabilities of Carbon Nanotubes from Atomic Increments, *Future Generation Comput. Syst.* **2004**, *20*, 763–772.

[38] L. Jensen, O. H. Schmidt, K. V. Mikkelsen, and P.–O. Åstrand, Static and Frequency–Dependent Polarizability Tensors for Carbon Nanotubes, *J. Phys. Chem. B* **2000**, *104*, 10462–10466.

[39] X. Blasé, L. X. Benedict, E. L. Shirley, and S. G. Louie, Hybridization Effects and Metallicity in Small Radius Carbon Nanotubes, *Phys. Rev. Lett.* **1994**, *72*, 1878–1881.

[40] S. Niyogi, M. A. Hamon, H. Hu, B. Zhao, P. Bhowmik, R. Sen, M. E. Itkis, and R. C. Haddon, Chemistry of Single–Walled Carbon Nanotubes, *Acc. Chem. Res.* **2002**, *35*, 1105–1113.

[41] S. Pinsuwan, P. B. Myrdal, Y.–C. Lee, and S. H. Yalkowsky, AQUAFAC 5: Aqueous Functional Group Activity Coefficients; Application to Alcohols and Acids, *Chemosphere* **1997**, *35*, 2503–2513.

[42] W. Feng, F. Zhou, X.–G. Wang, M.–X. Wan, A. Fujii, and K. Yoshino, Water–Soluble Multi–Walled Nanotube and its Film Characteristics, *Chin. Phys. Lett.* **2003**, *20*, 753–755.

[43] F. Torrens, Calculation of Organic Solvent–Water Partition Coefficients of Iron–Sulphur Protein Models, *Polyhedron* **2002**, *21*, 1357–1361.

[44] A. Kantola, H. O. Villar, and G. H. Loew, Atom Based Parametrization for a Conformationally Dependent Hydrophobic Index, *J. Comput. Chem.* **1991**, *12*, 681–689.

[45] A. Leo and C. Hansch, Linear Free–Energy Relationships between Partitioning Solvent Systems, *J. Org. Chem.* **1971**, *36*, 1539–1544.

[46] W. A. Scrivens and J. M. Tour, Potent Solvents for C_{60} and Their Utility for the Rapid Acquisition of ^{13}C NMR Data for Fullerenes, *J. Chem. Soc., Chem. Commun.* **1993**, 1207–1209.

[47] R. S. Ruoff, D. S. Tse, R. Malhotra, and D. C. Lorents, Solubility of Fullerene (C_{60}) in a Variety of Solvents, *J. Phys. Chem.* **1993**, *97*, 3379–3383.

[48] M. R. Diehl, S. N. Yaliraki, R. A. Beckman, M. Barahona, and J. R. Heath, Self–assembled, Deterministic Carbon Nanotube Wiring Networks, *Angew. Chem., Int. Ed. Engl.* **2002**, *41*, 353–356.

Biographies

Francisco Torrens is lecturer of physical chemistry at the Universitat de València. After obtaining a Ph.D. degree in molecular associations in azines and macrocycles from the Universitat de València, Dr. Torrens undertook postdoctoral research with Professor Rivail at the Université de Nancy I. More recently, Dr. Torrens has collaborated on projects with Professor Tomás–Vert. Major research projects include characterization of the electronic structure of electrically conductive organic materials, theoretical study of new electrically conductive organic materials, modellization of proteins, electronic correlation, development and applications of high–precision mono and multireferential electronic correlation methods, and development and application of high–precision quantum methods. Scientific accomplishments include the first implementation in a computer at the Universitat de València of a program for the elucidation of crystallographic structures, and the construction of the first computational–chemistry program adapted to a vector–facility supercomputer at a Spanish university.